A surface heat island study of Athens using high-resolution satellite imagery and measurements of the optical and thermal properties of commonly used building and paving materials

Article *in* International Journal of Sustainable Energy · September 2009

DOI: 10.1080/14786450802452753

6 authors, including:

Marina I. Stathopoulou
National and Kapodistrian University of Athens

Afroditi Synnefa
National and Kapodistrian University of Athens

Constantinos Cartalis
National and Kapodistrian University of Athens

Mat Santamouris
National and Kapodistrian University of Athens

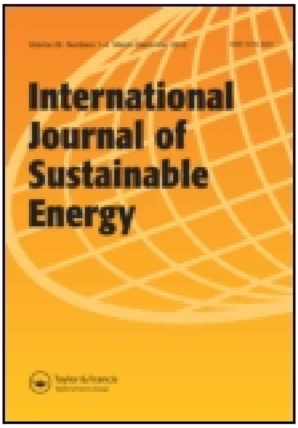

International Journal of Sustainable Energy
Publication details, including instructions for authors and subscription information:
http://www.tandfonline.com/loi/gsol20

A surface heat island study of Athens using high-resolution satellite imagery and measurements of the optical and thermal properties of commonly used building and paving materials

M. Stathopoulou [a] , A. Synnefa [a] , C. Cartalis [a] , M. Santamouris [a] , T. Karlessi [a] & H. Akbari [b]

[a] Division of Environmental Physics and Meteorology, Department of Physics, National and Kapodistrian University of Athens, Athens, Greece

[b] Lawrence Berkeley National Laboratory, Heat Island Group, Berkeley, CA, USA

Version of record first published: 04 Dec 2010.

To cite this article: M. Stathopoulou , A. Synnefa , C. Cartalis , M. Santamouris , T. Karlessi & H. Akbari (2009): A surface heat island study of Athens using high-resolution satellite imagery and measurements of the optical and thermal properties of commonly used building and paving materials, International Journal of Sustainable Energy, 28:1-3, 59-76

To link to this article: http://dx.doi.org/10.1080/14786450802452753

International Journal of Sustainable Energy
Vol. 28, Nos. 1–3, March–September 2009, 59–76

A surface heat island study of Athens using high-resolution satellite imagery and measurements of the optical and thermal properties of commonly used building and paving materials

M. Stathopoulou[a]*, A. Synnefa[a], C. Cartalis[a], M. Santamouris[a], T. Karlessi[a] and H. Akbari[b]

[a]*Division of Environmental Physics and Meteorology, Department of Physics, National and Kapodistrian University of Athens, Athens, Greece;* [b]*Lawrence Berkeley National Laboratory, Heat Island Group, Berkeley, CA, USA*

High-spatial resolution multispectral satellite images collected over the metropolitan Athens area in Greece were used to generate (a) a shortwave albedo map depicting the albedo spatial variations across the metropolitan area, (b) a fractional vegetation cover map showing the spatial distribution of urban vegetation and (c) a daytime and night-time land surface temperature (LST) map depicting the spatial variations of the surface temperature across the city. From LST maps, cooling and heating regions were identified and analysed to reveal relationships between surface heat islands and urban surface characteristics. Based on the data acquired with the use of satellite images and in order to better define the heat island problem and the mitigation measures that need to be taken, the most common building and paving materials used in the urban fabric of Athens were examined. Their optical properties were measured using a UV/VIS/NIR spectrophotometer fitted with an integrating sphere, an emissometer and their thermal performance was evaluated. Furthermore, measurements of the spectral reflectance help explore the possibility of increasing the near-infrared reflectance of materials in order to increase their total solar reflectance. The solar reflectance index of the samples was calculated in order to characterise them as 'cool' or 'warm'. Cool materials, with high albedo and thermal emittance values, attain lower surface temperatures when exposed to solar radiation, reducing the transference of heat to the environmental air.

Keywords: surface urban heat island; satellite remote sensing; cool materials; spectral reflectance; infrared emittance

1. Introduction

The Athens metropolitan area is experiencing rapid population growth, urban sprawl and a strong heat island. According to 2001 Greek census and housing data, the population of Athens rose to 2,664,776 inhabitants, which is 24.3% of the total population of Greece, and the building density in the central Athens area reached up to 5394 buildings/km^2. Population growth and high building density were some of the major drivers of urban sprawl. As a result, during the period 1990–2000, urbanised areas of Athens increased by 4.6% and newly urban districts were developed at the north, east and west of the Athens basin. Yet, changes in land use contribute to changes in the land surface characteristics as well. Materials commonly used in urban areas, such as concrete and asphalt, have significantly different thermal properties (heat capacity/thermal inertia) and surface radiative properties (albedo and emissivity) than the surrounding rural areas.

*Corresponding author. Email: mstathop@phys.uoa.gr

ISSN 1478-6451 print/ISSN 1478-646X online

DOI: 10.1080/14786450802452753
http://www.informaworld.com

As vegetation and natural surfaces are replaced by asphalt and concrete surfaces for roads, buildings and other structures necessary to accommodate growing populations, heat islands are developed; urban materials alter the energy balance of an urban surface as they absorb, rather than reflect, the incoming solar radiation causing surface temperatures and overall ambient temperatures to rise. Lack of vegetation in urban areas also affects the energy balance, as the natural cooling of the surface by evapotranspiration is minimised.

Athens is characterised by a strong heat island. This is supported by several studies that investigated the heat island of Athens by means of under-the-urban-canopy air temperature data collected from fixed or mobile weather stations (Cartalis *et al.* 2001, Santamouris *et al.* 2001, Livada *et al.* 2002, Mihalakakou *et al.* 2004). For example, in the study by Santamouris *et al.* (2001), which was based on air temperature measurements recorded from almost 30 urban and suburban stations located within the Athens basin, it was found that the heat island of Athens develops during both summer time and winter time. Especially in summer, the daily heat island intensity (defined as the maximum air temperature difference between urban and rural areas) may reach up to 10°C for the central urban regions, whereas the nocturnal heat island may rise up to 5°C. These results provide a quantitative measure of the increase in air temperature of urbanised Athens relative to its surrounding countryside. However, 'heat island' may also refer to the relative warmth of urban surfaces compared with their surrounding rural surfaces. In this case, the term *surface urban heat island* (SUHI) is used.

Satellite images recorded in the thermal infrared (TIR) part of the electromagnetic spectrum can be processed to define, at high spatial resolutions, the surface temperatures and display the SUHIs formed within a city. Moreover, images from satellite sensors operating in the visible and near-infrared wavelength regions can be utilised to extract the spatial distribution of urban albedo, emissivity and vegetation, which are important controls on SUHI development.

Many researchers have examined the SUHI effect by using satellite thermal images. Such SUHI studies are described in the reviews of Gallo *et al.* (1995), Voogt and Oke (2003) and Stathopoulou and Cartalis (2007a). However, only few studies exist that explore the SUHI intensity variation from daytime to night-time by means of satellite imagery. This arises from the fact that the number of available high spatial resolution satellite thermal images is limited when acquired at night-time in contrast to daytime. Relevant studies using low (Roth *et al.* 1989, Dousset and Gourmelon 2003), medium (Hung *et al.* 2006) and high spatial resolution satellite thermal data (Nichol 2005) have demonstrated that the relative intensity of the SUHI during daytime and night-time differs for the majority of the cities examined.

The objective of this study is two-fold: first to measure and map the daytime and night-time SUHI of Athens on the basis of high-resolution satellite thermal data and secondly to understand the causes for the development of the SUHI effect and find ways to mitigate its consequences by examining the optical and thermal properties of the most common building and paving materials used in the city. To achieve this, two thermal satellite images were utilised: 11 October 2003 night-time (23:32 land surface temperature (LST)) advanced spaceborne thermal emission and reflection sensor (ASTER) image and 12 October 2003 daytime (11:53 LST) thermal mapper (TM) image. The two images were selected for the following reasons: (a) the year 2003 is classified by the National Observatory of Athens as one of the six warmest years of Athens' temperature record, with October 2003 included among the 10 warmest Octobers of the record, (b) both images correspond to cloud-free atmospheric conditions with the daytime image recorded only 12 h later than the night-time image and (c) their thermal data have a spatial resolution of about 100 m (90 m for ASTER and 120 m for TM) which is considered an optimum scale for capturing the inter-urban surface temperature variations. The satellite data were utilised to quantify daytime and night-time surface temperature (T_s), albedo (α), normalised difference vegetation index (NDVI) vegetation fraction (f_v) and emissivity (ε) of Athens. The satellite-derived maps were used in turn to extract (i) detailed measurements of

T_s, α, f_v and ε (mean and standard deviation values) that occur for specific land covers across the metropolitan Athens landscape as reproduced from the Corine Land Cover 2000 (CLC00) database for Greece: urban/densely built, suburban/medium built, industrial/commercial, urban use, agriculture and forest and (ii) the changes in T_s of these land covers between day and night. Furthermore, daytime (11:53 LST) and night-time (23:32 LST) SUHI intensities of Athens were estimated expressed as the difference in mean T_s between the urban and non-urban land covers.

On the other hand, 87 building and paving materials commonly used in the urban fabric of Athens were selected and studied. Taking into account that two main properties affecting the temperature of a surface are the solar reflectance (SR) and the infrared emittance (Rosenfeld *et al.* 1996, Akbari *et al.* 1997, Bretz and Akbari 1997), measurements of these properties were taken along with surface temperature measurements for the selected materials.

In the literature, several studies report the SR and the thermal performance of various roofing materials. Simpson and McPherson (1997) found that white roofs (~0.75 albedo) were up to 20°C cooler than grey (~0.30 albedo) or silver (~0.50 albedo) and up to 30°C cooler than brown roofs (~0.10 albedo). Parker *et al.* (2000) measured the optical properties of 60 roofing materials and report that asphalt shingles are characterised by low SR values (0.03–0.26), white elastomeric coatings are characterised by high SR values (0.65–0.78) and finally white concrete tiles and metal roofs have quite high values of SR (0.73 and 0.67, respectively). Prado and Ferreira (2005) report the albedo for various roofing materials and also the temperature that each material can reach when exposed to solar radiation. Researchers at the Lawrence Berkeley National Laboratory (LBNL) have created a database (http://eetd.lbl.gov/coolroof/) that reports the SR, the infrared emittance and the temperature rise of various commonly used roofing materials, aiming to assist with the selection of more appropriate roofing materials. Regarding the optical properties and thermal performance of paving materials, only a few studies exist concluding mainly that asphalt shows lower surface temperatures than concrete (Asaeda *et al.* 1996, Santamouris *et al.* 2001). Doulos *et al.* (2004) studied the thermal performance of 93 commonly used pavement materials. It was found that tiles made of marble, mosaic and stone were cooler than the tiles made of concrete pavestone and asphalt.

Here, the SR and infrared emittance of both roofing and paving materials have been measured. Furthermore, the spectral reflectance of these materials is also reported. Knowledge of the spectral reflectance of existing materials allows researchers and manufacturers to explore the possibility of increasing their SR by using near-infrared reflective colour pigments. These pigments can produce the same colour but offer increased SR, as they are more reflective in the near-infrared region of the solar spectrum (0.7–2.5 μm), than conventional pigments (Akbari *et al.* 2004, Synnefa *et al.* 2007).

Increasing the SR of a surface of the building envelope lowers its temperature, which in turn decreases the heat penetrating into the building, thus decreasing the cooling energy use and improving the thermal comfort conditions inside the building (Akbari *et al.* 1997). If it is a surface of the urban environment, it contributes to decrease the temperature of the ambient air, as heat convection intensity from a cooler surface is lower (Sailor 1995, Taha *et al.* 2000, 2002). Therefore, the use of high albedo urban surfaces is an inexpensive measure that can reduce summertime temperatures. In order to make appropriate choices, when selecting materials for buildings or other outdoor urban spaces, it is important to know the optical properties and thermal performance of available materials.

2. Processing of the satellite and land cover data

Different processing techniques were applied to visible and TIR satellite data for deriving the urban components, as images from two different satellite sensors were utilised (Table 1). Both

Table 1. List of the satellite images used in this study.

Satellite/sensor	Acquisition date	Acquisition time	Component-derived	Spatial resolution (m)
Terra/ASTER	11/10/2003	23:32 LST	Night-time surface temperature	90
Landsat 5/TM	12/10/2003	11:53 LST	Daytime surface temperature	120
			Vegetation fraction cover	30
			Total shortwave albedo (0.25–5.1 μm)	30
			Surface emissivity (10–12 μm)	30

images correspond to cloud-free days of similar climatic conditions. Specifically, the average relative humidity values on the 11th and 12th of October were 49 and 48%, respectively, whereas the mean daily air temperature was 17.8°C on both days. The climatic data were collected from the meteorological station of the National Observatory of Athens located at Thissio (37°58′N, 23°43′E) near the centre of Athens.

2.1. *Satellite data*

Landsat 5 was launched in 1984. Since then, the satellite has operated from a sun-synchronous, near-polar orbit, collecting images of the same site every 16 days. The TM sensor onboard Landsat 5 acquires image data in seven bands ranging from the visible part of the electromagnetic spectrum to the mid-infrared with a 30 m spatial resolution. One thermal band is also included having a 120 m spatial resolution. The wavelengths of the spectrum captured by each TM band are shown in Table 2. The Terra spacecraft also operates in a sun-synchronous, near-polar orbit at an altitude of 705 km. The orbit parameters are the same as Landsat 5 except for the equatorial local crossing time; Terra is about 45 min behind Landsat 5. The ASTER sensor onboard Terra covers a spectral region with 14 bands from the visible to the TIR with spatial resolutions that are generally more detailed than those of the TM sensor. Specifically, the spatial resolution varies with wavelength: 15 m in the visible and infrared (VNIR), 30 m in the short-wave infrared (SWIR) and 90 m in the TIR (Table 3). Another advantage of ASTER is that its night-time acquisitions are more easily available than those of the TM sensor.

2.1.1. *Calibration procedure*

For the TM sensor, conversion of the digital number (DN_i) values of the image band i to at-sensor spectral radiance (L_i) values was performed by using the gain (G) and offset (B) values supplied

Table 2. Characteristics of the TM sensor.

Spectral bands	Wavelength range (μm)	Spatial resolution (m)
Band 1: blue	0.45–0.52	30
Band 2: green	0.52–0.60	30
Band 3: red	0.63–0.69	30
Band 4: NIR	0.76–0.90	30
Band 5: MIR	1.55–1.75	30
Band 6: TIR	10.40–12.50	120
Band 7: MIR	2.08–2.35	30

NIR, near-infrared; MIR, mid-infrared; TIR, thermal-infrared.

Table 3. Characteristics of the ASTER sensor.

ASTER sensor	Bands	Wavelength range (μm)	Spatial resolution (m)
VNIR	1	0.52–0.60	15
	2	0.63–0.69	
	3N	0.78–0.86	
	3B	0.78–0.86	
SWIR	4	1.60–1.70	30
	5	2.145–2.185	
	6	2.185–2.225	
	7	2.235–2.285	
	8	2.295–2.365	
	9	2.360-2.430	
TIR	10	8.125–8.475	90
	11	8.475–8.825	
	12	8.925–9.275	
	13	10.25–10.95	
	14	10.95–11.65	

in the image header file (Chander and Markham 2003):

$$L_i = G \times \mathrm{DN}_i + B \quad (\mathrm{W/m^2\,sr\,\mu m}). \tag{1}$$

In the case of ASTER, calibration of the thermal band (ASTER-13) was performed by using the following equation (Earth Remote Sensing Data Center 2001)

$$L_{13} = 5.693 \times 10^{-3} \cdot (\mathrm{DN}_{13} - 1). \tag{2}$$

As a next step, the at-sensor spectral radiance values L_i of the TM reflective bands ($i = 1\text{–}5, 7$) were converted to at-sensor (or planetary) spectral reflectance (ρ_i) by applying the following equation

$$\rho_i = \frac{\pi \cdot L_i \cdot d^2}{\mathrm{ESUN}_i \cdot \cos\vartheta}, \tag{3}$$

where L_i is the at-sensor spectral radiance as computed from Equation (1), d the mean distance between the Earth and the Sun (in astronomical units), ESUN_i the mean solar exoatmospheric irradiance in TM bands ($\mathrm{W/m^2\,\mu m}$) and ϑ the solar zenith angle (in radians). Additionally, the at-sensor radiance values of the TM thermal image data (band 6) were converted to at-sensor brightness temperature (BT_i) values by inverting the Planck equation

$$\mathrm{BT}_i = \frac{c_2}{\lambda \cdot \ln((c_1 \cdot \lambda^{-5}/L_i) + 1)} \quad (\mathrm{K}), \tag{4}$$

where λ is the effective wavelength for TM6 in microns, c_1 the first radiation constant ($1.19104 \times 10^8\,\mathrm{W\,\mu m^4\,m^{-2}\,sr^{-1}}$), c_2 the second radiation constant ($1.43877 \times 10^4\,\mathrm{\mu m\,K}$) and L_i is the at-sensor radiance values of TM6 as computed from Equation (1).

2.1.2. *Surface albedo α retrieval*

Planetary reflectance of Equation (3) accounts for the combined reflectance of the surface and the atmosphere. Therefore, additional correction of the reflective TM bands image data was required to eliminate the atmospheric effects and compute the spectral surface reflectances. Atmospheric correction was implemented using the COST method developed by Chavez (1996). The major advantage of this method is that it corrects for both solar and atmospheric effects based solely on the image data requiring no *in situ* atmospheric field measurements during the satellite overflight. According to the method, surface reflectances ($s\rho_i$) can be obtained from the at-sensor reflectances ρ_i by applying the equation that follows:

$$s\rho_i = \frac{\pi \cdot (L_i - L_{\mathrm{haze},i}) \cdot d^2}{\mathrm{ESUN}_i \cdot \cos\vartheta \cdot \tau}, \tag{5}$$

where $s\rho_i$ is the surface reflectance for the reflective TM band i, L_i the at-sensor spectral radiance, d the mean distance between the Earth and the Sun (in astronomical units), ESUN_i the mean solar exoatmospheric irradiance in the reflective TM band i (W/m^2 µm), ϑ the solar zenith angle, $\tau(= \cos\theta)$ the atmospheric transmittance along the path from the sun to the ground surface and $L_{\mathrm{haze},i}$ the path radiance for the reflective band i (given as the non-zero radiance received at the sensor from dark objects within the image due to atmospheric scattering (Chavez 1988)).

The COST method was applied to the raw DN values of the reflective TM image data from which atmospherically corrected surface reflectances for bands TM1-5 and TM7 were derived. Surface reflectances were used thereafter for computing the total shortwave (0.25–5.1 µm) albedo α of the surface. The conversion was accomplished by applying the formula developed by Liang (2000):

$$\alpha = 0.356 \cdot s\rho_1 + 0.13 \cdot s\rho_3 + 0.373 \cdot s\rho_4 + 0.085 \cdot s\rho_5 + 0.072 \cdot s\rho_7, \tag{6}$$

where $s\rho_i$ is the surface reflectance for the reflective TM band i.

2.1.3. *Vegetation fraction cover f_{v} retrieval*

The NDVI measures the greenness of the environment and the amount of vegetation present. A higher NDVI indicates a higher degree of greenness and healthy vegetation; for example, an NDVI value of 0 corresponds to no vegetation, whereas a value of 1 designates a surface being 100% vegetative. The NDVI index was computed by using the surface reflectance values from the TM3 and TM4 bands as follows:

$$\mathrm{NDVI} = \frac{s\rho_4 - s\rho_3}{s\rho_4 + s\rho_3}. \tag{7}$$

Fractional vegetation cover (f_{v}) expresses the portion of the pixel covered by vegetation. The vegetation cover fraction can be computed through the NDVI index from Equation (8)

$$f_{\mathrm{v}} = \left(\frac{\mathrm{NDVI}_i - \mathrm{NDVI}_{\min}}{\mathrm{NDVI}_{\max} - \mathrm{NDVI}_{\min}}\right)^2, \tag{8}$$

where NDVI_i is the NDVI value of image pixel i and $\mathrm{NDVI}_{\min}$, $\mathrm{NDVI}_{\max}$ are the minimum and maximum NDVI values of the image. It takes values within the range of [0, 1].

2.1.4. *Surface emissivity ε retrieval*

Surface emissivity plays a significant role in LST estimation. To obtain accurate LST values and consequently differences in T_{s} observed between various types of land cover found within a certain landscape, the land surface emissivity over the examined area must be determined. In this study, effective emissivity in the 10–12 µm waveband was computed using the method of

Caselles *et al.* (1991). According to this method, pixels are considered to be composited of urban and vegetation surfaces and their effective emissivity can be obtained as:

$$\varepsilon = (1 - f_{\mathrm{v}}) \cdot \varepsilon_{\mathrm{c}} + f_{\mathrm{v}} \cdot \varepsilon_{\mathrm{v}}, \tag{9}$$

where f_{v} is the vegetation fraction cover, ε_{c} the mean emissivity of the city considered (represented by densely urbanised areas) and ε_{v} the emissivity of vegetation. Assuming mean emissivity values of 0.93 for the city of Athens and 0.98 for vegetation (Stathopoulou *et al.* 2007), Equation (9) was applied to the TM data resulting to the production of a surface emissivity map of the metropolitan Athens area having a 30 m spatial resolution.

2.1.5. *LST retrieval*

LST (T_{s}) was computed based on the generalised single-channel algorithm developed by Jiménez-Munõz and Sobrino (2003). The reason for adopting this algorithm among others published in the literature is that the specific algorithm can be applied to different thermal sensors using the same equation and coefficients. Therefore, the same algorithm can be used in order to derive surface temperature from both TM and ASTER thermal data. The expression for T_{s} (in Kelvin) is given as:

$$T_{\mathrm{s}} = \gamma(\lambda, T_0) \cdot \left\{ \frac{\psi_1(\lambda, w) \cdot L_{\lambda}^{\text{at-sensor}} + \psi_2(\lambda, w)}{\varepsilon_{\lambda}} + \psi_3(\lambda, w) \right\} + \delta(\lambda, T_0), \tag{10}$$

where

$$\gamma(\lambda, T_0) = \left\{ \frac{c_2 \cdot B(\lambda, T_0)}{T_0^2} \left[\frac{\lambda^4}{c_1} \cdot B(\lambda, T_0) + \frac{1}{\lambda} \right] \right\}^{-1}, \tag{11}$$

$$\delta(\lambda, T_0) = T_0 - \frac{T_0^2}{c_2 \cdot \left[\lambda^4/c_1 \cdot B(\lambda, T_0) + 1/\lambda \right]}. \tag{12}$$

In the above equations, λ is the effective wavelength for the band considered in μm, c_1 the first radiation constant ($1.19104 \times 108\,\mathrm{W}\,\mu\mathrm{m}^4/\mathrm{m}^2$ sr) and c_2 the second radiation constant ($1.43877 \times 10^4\,\mu\mathrm{m\,K}$). In Equation (10), ε_{λ} is the land surface emissivity, whereas ψ_1, ψ_2 and ψ_3 are the atmospheric functions. Their formula is given as:

$$\psi_k = \eta_{k\lambda} w^3 + \xi_{k\lambda} w^2 + \chi_{k\lambda} w + \varphi_{k\lambda} \quad (k = 1, 2, 3), \tag{13}$$

where w is the water vapour content in g/cm^2 and $\eta_{k\lambda}$, $\xi_{k\lambda}$, $\chi_{k\lambda}$ and $\varphi_{k\lambda}$ are spectral functions with three-degree dependence on the wavelength λ, which can be computed from the following expressions:

$$\eta_{k\lambda} = a_3^{(k)}\lambda^3 + a_2^{(k)}\lambda^2 + a_1^{(k)}\lambda + a_0^{(k)}, \tag{14}$$

$$\xi_{k\lambda} = b_3^{(k)}\lambda^3 + b_2^{(k)}\lambda^2 + b_1^{(k)}\lambda + b_{\mathrm{o}}^{(k)}, \tag{15}$$

$$\chi_{k\lambda} = c_3^{(k)}\lambda^3 + c_2^{(k)}\lambda^2 + c_1^{(k)}\lambda + c_{\mathrm{o}}^{(k)}, \tag{16}$$

$$\varphi_{k\lambda} = d_3^{(k)}\lambda^3 + d_2^{(k)}\lambda^2 + d_1^{(k)}\lambda + d_{\mathrm{o}}^{(k)}. \tag{17}$$

The numerical coefficients used in Equations (14–17) ($a_j^{(k)}, b_j^{(k)}, c_j^{(k)}, d_j^{(k)}$; $j = 0, 3$ and $k = 1, 3$) for the 10–12 μm spectral region can be found in Jiménez-Munõz and Sobrino (2003). The reader may refer to their paper for more details.

The term T_0 included in Equations (10–12) is defined as a temperature value near to the T_s value. As noted by Jiménez-Munõz and Sobrino (2003), if the atmospheric water vapour content is low, then T_0 can be approximated by the brightness temperature BT. Consequently, $B(\lambda, T_0)$ is equal to the at-sensor spectral radiance L. Given that, for Athens, the mean monthly water vapour content value of October is $2\,\mathrm{g/cm^2}$ (Chrysoulakis and Cartalis 2002), the above approach was adopted in this study. Therefore, for both sensors (ASTER and TM), LST values were obtained from Equation (10) by using a water vapour content value of $2\,\mathrm{g/cm^2}$ and the emissivity values computed as described in Section 2.1.4. Thus, spatial distribution maps of daytime and night-time LST for the city of Athens were produced.

2.2. *Land cover data*

To link the spatial patterns of daytime and night-time surface temperature, albedo, emissivity and the vegetation of Athens with the land surface characteristics, the Corine Land Cover 2000 (CLC00) database for Greece was utilised. The CLC00 is a geographic land cover/land use database produced by the European Environment Agency that describes land cover/land use according to a nomenclature of 44 classes organised in three levels of detail (European Commission 1994). The database was provided in a vector-based format and a UTM/WGS84 projection. As our interest focused on determining the T_s differences between urban surfaces and rural ones, the main CLC00 category of *artificial surfaces*, including 11 detailed urban land covers and uses (Table 4), was re-organised to form new land cover classes based on similar land cover structure characteristics. In this context, *discontinuous urban fabric*, *green urban areas* and *sport and leisure facilities* of *artificial surfaces* were grouped together forming a new class named *suburban/medium built*. Likewise, *transport units* and *mine, dump and construction sites* are united into one class called *urban use*. The new classification performed is shown analytically in Table 4.

As a result, the metropolitan Athens landscape was classified into six land covers, of which two represent the residential regions (urban/densely built, suburban/medium), two represent the developed regions (industrial/commercial, urban use) and two represent the rural surroundings of the city (agriculture, forest). Therefore, a new vector map was produced providing the geographical distribution of each land cover class within the metropolitan Athens area (Figure 1).

In the following, all the components derived from the ASTER and TM images were geometrically corrected to the land cover vector map so as to ascertain accurate co-registration between the data sets. Then, the land cover vector map was overlaid on the satellite-derived maps of each

Table 4. Original CLC00 and new grouped land cover classes.

CLC2000 class code	New class code	Label
1.1.1. Continuous urban fabric	1	Urban/densely built
1.1.2. Discontinuous urban fabric	2	Suburban/medium built
1.2.1. Industrial/commercial units	3	Industrial/commercial
1.2.2. Road/rail networks & associated land	4	Urban use
1.2.3. Port areas	4	Urban use
1.2.4. Airports	4	Urban use
1.3.1. Mineral extraction sites	4	Urban use
1.3.2. Dump sites	4	Urban use
1.3.3. Construction sites	4	Urban use
1.4.1. Green urban areas	2	Suburban/medium built
1.4.2. Sport and leisure facilities	2	Suburban/medium built
2. Agricultural areas	5	Agriculture
3. Forests and semi-natural areas	6	Forest

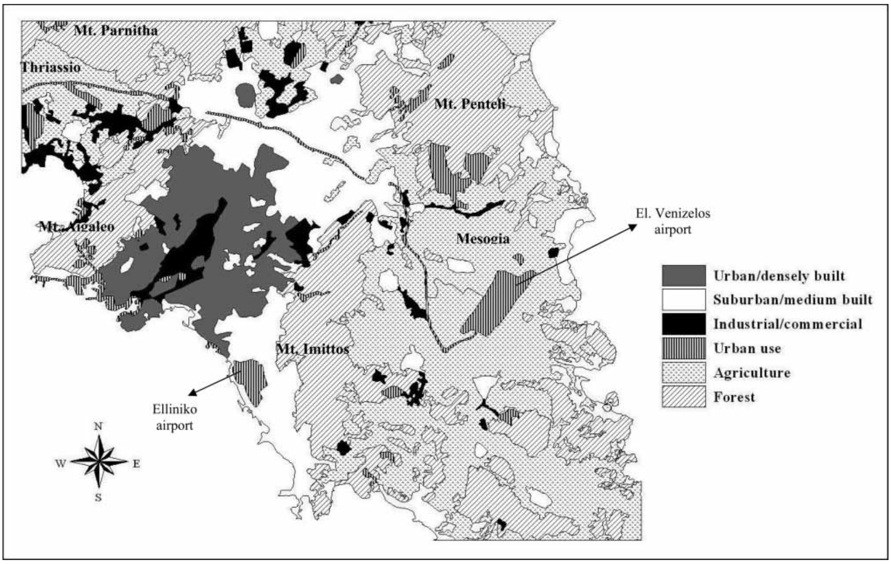

Figure 1. CLC00 reproduced land cover map for the metropolitan Athens area.

Table 5. Statistics (mean and standard deviation values) for each of the five components derived from the satellite data by land cover class.

	Land cover class	$f_v \pm$ sd	$\alpha \pm$ sd	$\varepsilon \pm$ sd	$T_s \pm$ sd (daytime)	$T_s \pm$ sd (night-time)
Urban	Urban/densely built	0.236 ± 0.097	0.147 ± 0.026	0.942 ± 0.005	299.93 ± 1.28	293.13 ± 1.21
	Suburban/medium built	0.360 ± 0.141	0.151 ± 0.035	0.948 ± 0.007	299.62 ± 2.10	290.89 ± 1.96
	Industrial/commercial	0.269 ± 0.144	0.159 ± 0.043	0.943 ± 0.007	302.17 ± 2.41	290.43 ± 2.37
	Urban use	0.258 ± 0.122	0.177 ± 0.059	0.943 ± 0.006	302.67 ± 2.91	290.88 ± 2.65
Rural	Agriculture	0.400 ± 0.121	0.152 ± 0.029	0.950 ± 0.006	302.15 ± 2.32	288.93 ± 1.95
	Forest	0.474 ± 0.147	0.127 ± 0.045	0.954 ± 0.007	300.13 ± 3.59	289.78 ± 2.15

component and by applying a GIS zonal summary technique, statistics of each component by land cover class were extracted (Table 5).

Satellite-derived maps of albedo (Figure 2), of fractional vegetation cover (Figure 3), surface emissivity (Figure 4), daytime LST (Figure 5) and night-time LST (Figure 6) over the metropolitan Athens area are provided below.

3. Analysis of the satellite SUHI results

On the daytime image (Figure 5), surface temperature spatial patterns reveal the development of a 'negative' SUHI or a *surface urban cool island* where urban surfaces appear to be relatively cooler than the surrounding rural surfaces. The phenomenon is not only evidenced by the visual inspection of the T_s image produced from the TM sensor, but it is also supported by the statistical results given in Table 5. Therefore, urban/densely built and suburban/medium built surfaces were found to be about 1°C cooler than rural surfaces, leading to a negative SUHI with a mean value of 1°C and a maximum value of 5.85°C at that time of day (11:53 LST). Additionally, industrial/commercial surface areas as well as urban use surface areas were found to be about

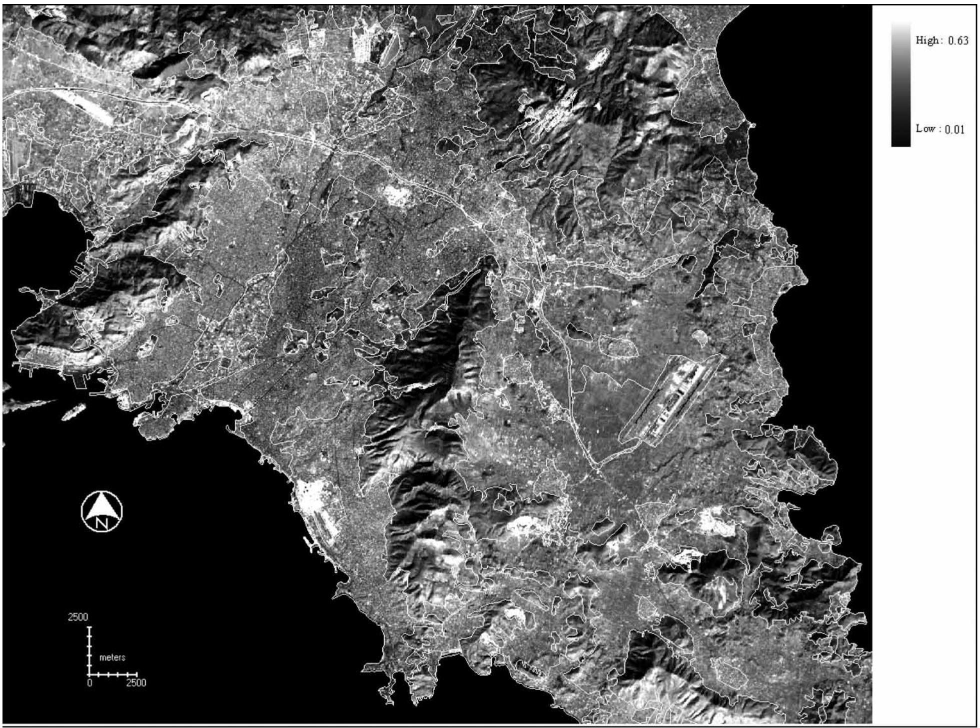

Figure 2. Shortwave albedo map of metropolitan Athens at 30 m spatial resolution. Land cover map is overlaid.

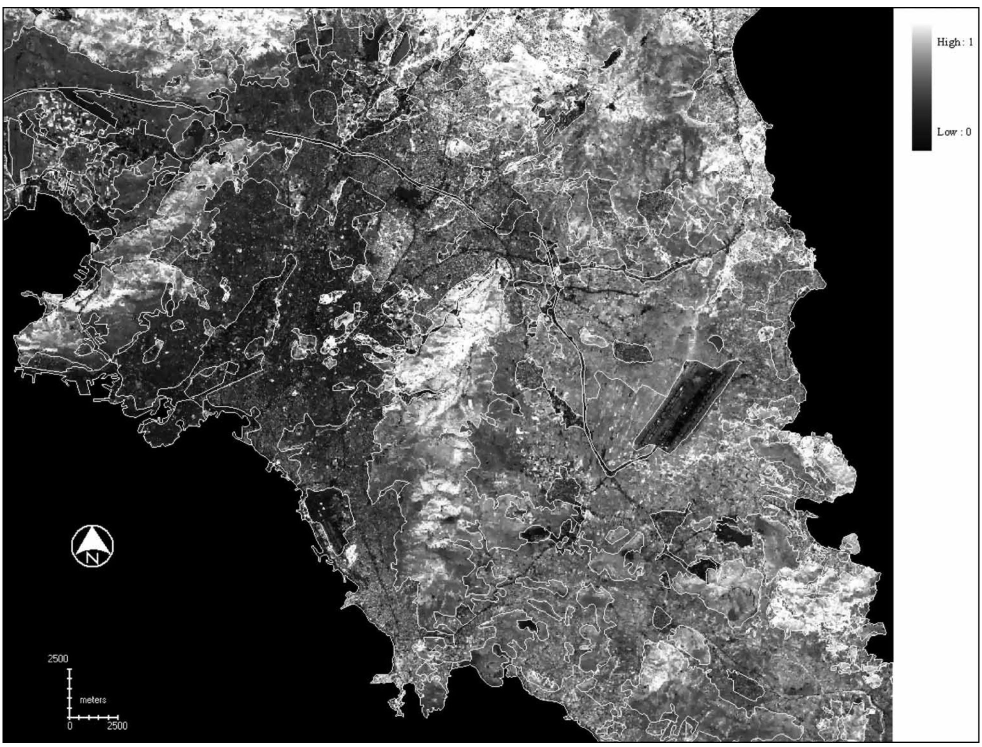

Figure 3. Fractional vegetation cover map of metropolitan Athens at 30 m spatial resolution. Land cover map is overlaid.

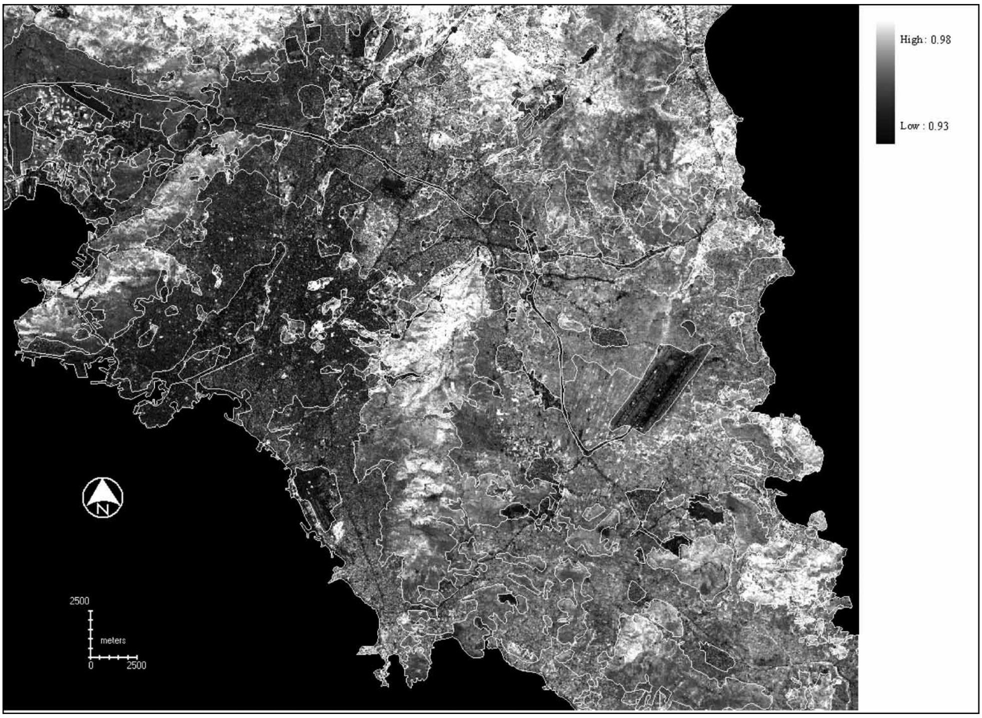

Figure 4. Surface emissivity map of metropolitan Athens at 30 m spatial resolution. Land cover map is overlaid.

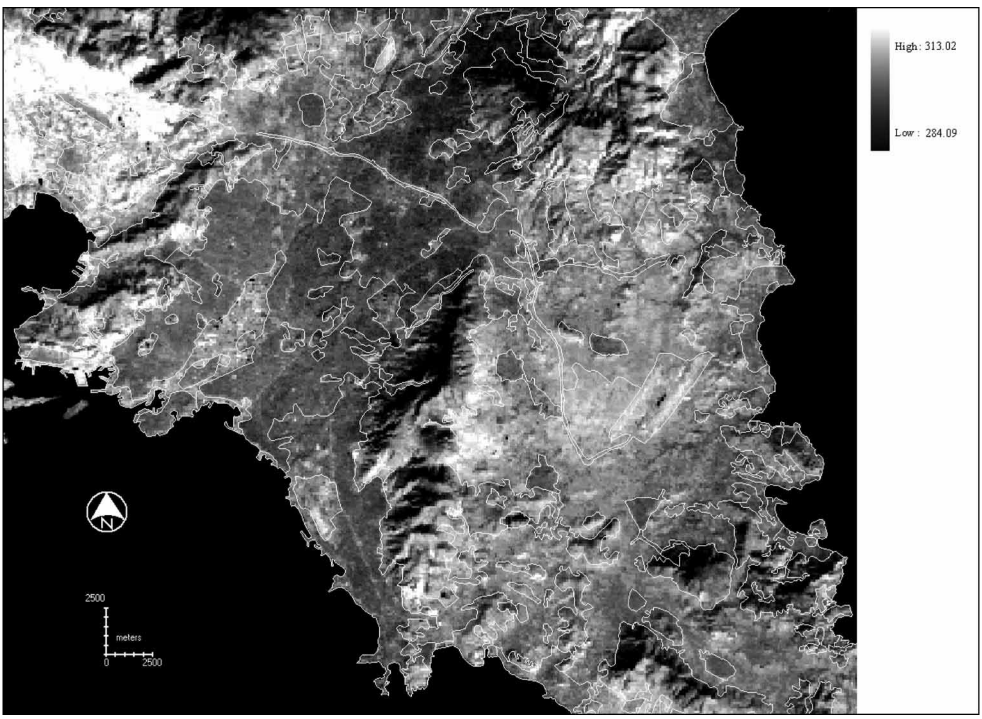

Figure 5. Daytime surface temperature (in Kelvin) of metropolitan Athens on 12 October 2003 at 11:53 LST as derived from the TM sensor. Land cover map is overlaid (white lines).

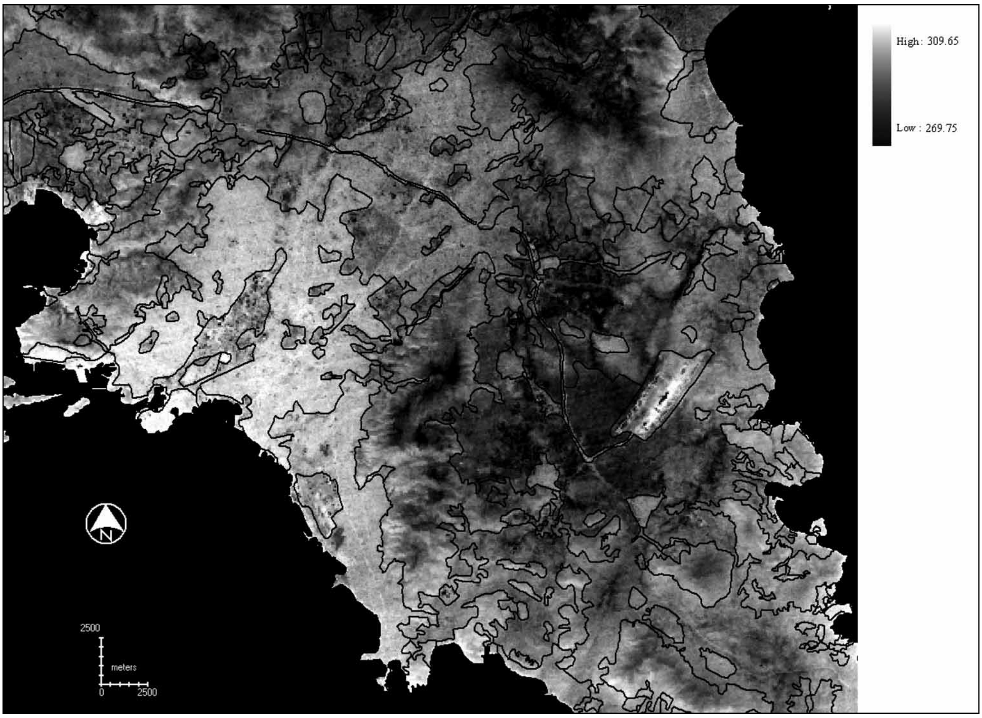

Figure 6. Night-time surface temperature (in Kelvin) of metropolitan Athens on 11 October 2003 at 23:32 LST as derived from the ASTER sensor. Land cover map is overlaid (black lines).

2.7°C warmer than the residential surface areas. Bright areas of high T_s values corresponding to the industrial/commercial units near the centre of Athens can be easily observed in Figure 5. High surface temperatures were also related to land covers as transport units (ports, airports) and mineral extraction sites. For example, the high surface temperatures of Elliniko airport, southwards near the coastline of Athens, are well distinct in Figure 5.

In general, it can be concluded that the thermal environment of Athens during daytime depends on the combined influence of the area topography and surface thermal characteristics. It must be noted that the daytime images of Landsat 5 recorded over the city of Athens are acquired at around 08:53 UTC (10:53 local winter time or 11:53 local summer time) when the solar height is still low. At that time of day, the Athens basin is partly shaded by the mountains eastwards; hence, it is less exposed to the sunlight contrast of the open plains of Mesogia and Thriassio at the east and west of the basin, respectively. As these surface areas are mainly composed of sparse low vegetation (particularly olive trees and vineyards) and bare soil, they become warm faster than urban surface areas which are extensively covered by building materials of high thermal capacity, such as concrete and asphalt. Assuming thermal inertia of surfaces as a measure of thermal mass per unit area, the lower warming rate of the residential urban surfaces (urban/densely built, suburban/medium built) compared to the industrial/commercial, urban use and rural surfaces observed at that time of day is explained. The influence of topography on the surface temperature pattern of Athens is further supported by the distinct differential warming of the E–W mountain slopes. As shown in Figure 5, the western slopes of Imittos, Penteli, Parnitha and Aigaleo appear to be cooler than the respective eastern ones.

During night-time, the surface thermal pattern of Athens is inverted as the higher surface temperatures are associated with the residential urban areas rather than the different urban use and rural areas (Figure 6). At night, in the absence of solar forcing, cooling or warming of a surface is inclusively determined by its thermal characteristics. Thus, at night-time, the urban/densely built surfaces of Athens were presented to be 4.3°C warmer than the surrounding rural surfaces, due to the higher thermal emissivity of the vegetated surfaces compared to concrete surfaces. This observed difference in T_s results in a strong night-time SUHI with an observed mean value of 4.3°C and a maximum value of 7.4°C at that time of night (23:32 LST). As shown in Figure 6, there is an observed differential warming between the urban/densely built and suburban/medium built surfaces, which is also supported by the statistical results given in Table 5. Thus, urban/densely built surfaces were measured to be about 2.24°C warmer than suburban/medium built surfaces due to higher building density (resulting in lower sky view factor), lower vegetation cover and thermal emissivity. Moreover, in contrast to daytime, the densely built surfaces of the city appear to be 2.7°C warmer than the industrial/commercial surface areas as they are characterised by lower vegetation cover and thermal emissivity. Notable are the cooler surface temperatures of Elliniko airport (ex-national) compared with the surrounding urban surfaces. As this is an open surface covered mostly by bare soil, it is characterised by thermal inertia. Thus, this surface area appears to be warmer and cooler than the surrounding urban surface areas in the daytime and night-time T_s images, respectively. Similar thermal characteristics appear to have the industrial/commercial surface areas of the urban core of Athens due to high coverage of bare soil. On the other hand, vegetative urban surfaces such as green urban areas and sport/leisure facilities are cool islands of the city, depicting lower surface temperatures during night-time than urban/densely built surfaces. In the Mesogia plains, the airport of Eleftherios Venizelos, its satellite urbanised suburbs and the highway of Attiki Odos connecting the airport of Eleftherios Venizelos with the western suburbs of Athens can be clearly observed as they all display higher T_s values than the surrounding agricultural surfaces. Such cases demonstrate the alteration of the natural thermal environment caused by the urban development and sprawl.

4. Experimental procedure

As mentioned earlier in this study, 87 paving and building materials were studied. These materials can be divided into 10 categories: (a) asphalt (old, new), (b) asphalt shingles, (c) concrete, (d) marble, (e) mosaic, (f) ceramic tiles, (g) stone, (h) rubber, (i) coatings and (j) membranes. In order to study the optical properties and the thermal performance of the materials, the following parameters were measured.

(a) The spectral reflectance of the samples was measured using a UV/VIS/NIR spectrophotometer (Varian Carry 5000) fitted with a 150 mm diameter, integrating sphere (Labsphere DRA 2500) that collects both specular and diffuse radiation. The reference standard reflectance material used for the measurement was a PTFE plate (Labsphere). The measurements were performed according to the ASTM Standard E903-96.
(b) The infrared emittance of the samples was also measured with the use of the Devices & Services emissometer model AE. This emittance device determines the total thermal emittance, in comparison with standard high and low emittance materials.

Some of the tested materials had a non-uniform surface (i.e. concrete tiles with a pattern, mosaic with two different colours and a rough surface, etc.). In order to overcome this problem several measurements were taken at various points on the surface of the sample and then an averaging procedure was performed. With this methodology, the results are more representative, although there is still an error introduced due to the non-uniformity of the surface for some materials.

5. Optical properties and thermal performance of the materials

The results of the spectrophotometric measurements were used in order to calculate the SR of each sample. The calculation was done by the weighted averaging method, using a standard solar spectrum as the weighting function. The spectrum employed is that suggested by ASTM (ASTM Standard E903-96, ASTM Standard G159-91). The maximum and minimum values of SR calculated for each material category are shown in Table 6. The SR varies according to the colour and the construction material. The values for the infrared emittance are also included in Table 6. For the majority of the materials tested, the infrared emittance is quite high (about 0.9) with the exception of the aluminum-pigmented coatings. This is because they contain aluminum flakes that have a very low emissivity.

High infrared emittance values reveal the ability of a warm or hot material to re-radiate some of its heat in the form of infrared radiation and therefore contribute to keeping a surface cooler. In Table 6, the range of the calculated surface temperature for each material category is also included. This calculation was based on the equation describing the thermal balance of a surface under the sun that is insulated underneath (Bretz *et al.* 1997), as is the case for the samples of this experiment:

$$(1 - a)I = \varepsilon\sigma(T_s^4 - T_{sky}^4) + h_c(T_s - T_a), \quad (18)$$

where a is the SR or albedo of the surface, I the total solar radiation incident on the surface ($I = 1000\,\mathrm{W/m^2}$), ε the emissivity of the surface, σ the Stefan–Boltzmann constant,

Table 6. Minimum and maximum values of the SR, infrared emittance and surface temperatures for each material category.

Material	SR	Infrared emittance	T_s(°C)
Asphalt	0.06–0.15	0.9	77.6–81.8
Asphalt shingles	0.03–0.18	0.91	75.1–83.5
Concrete	0.13–0.58	0.9	56.2–78.6
Marble	0.37–0.73	0.9	48.6–67.3
Mosaic	0.18–0.65	0.9	52.5–76.1
Ceramic tiles	0.38–0.56	0.9	57.2–66.4
Stone	0.20–0.75	0.9	47.5–75.1
Rubber	0.07	–	69.7
Coatings	0.04–0.84	0.35–0.93	42.9–83.3
Membranes	0.06–0.69	0.86–0.87	50.1–82.8

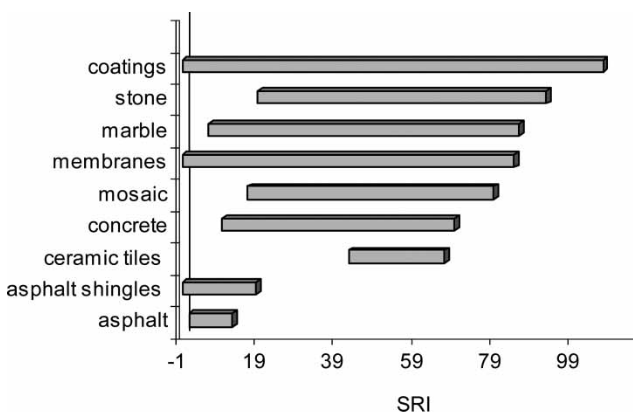

Figure 7. The range of the calculated SRI for each material category.

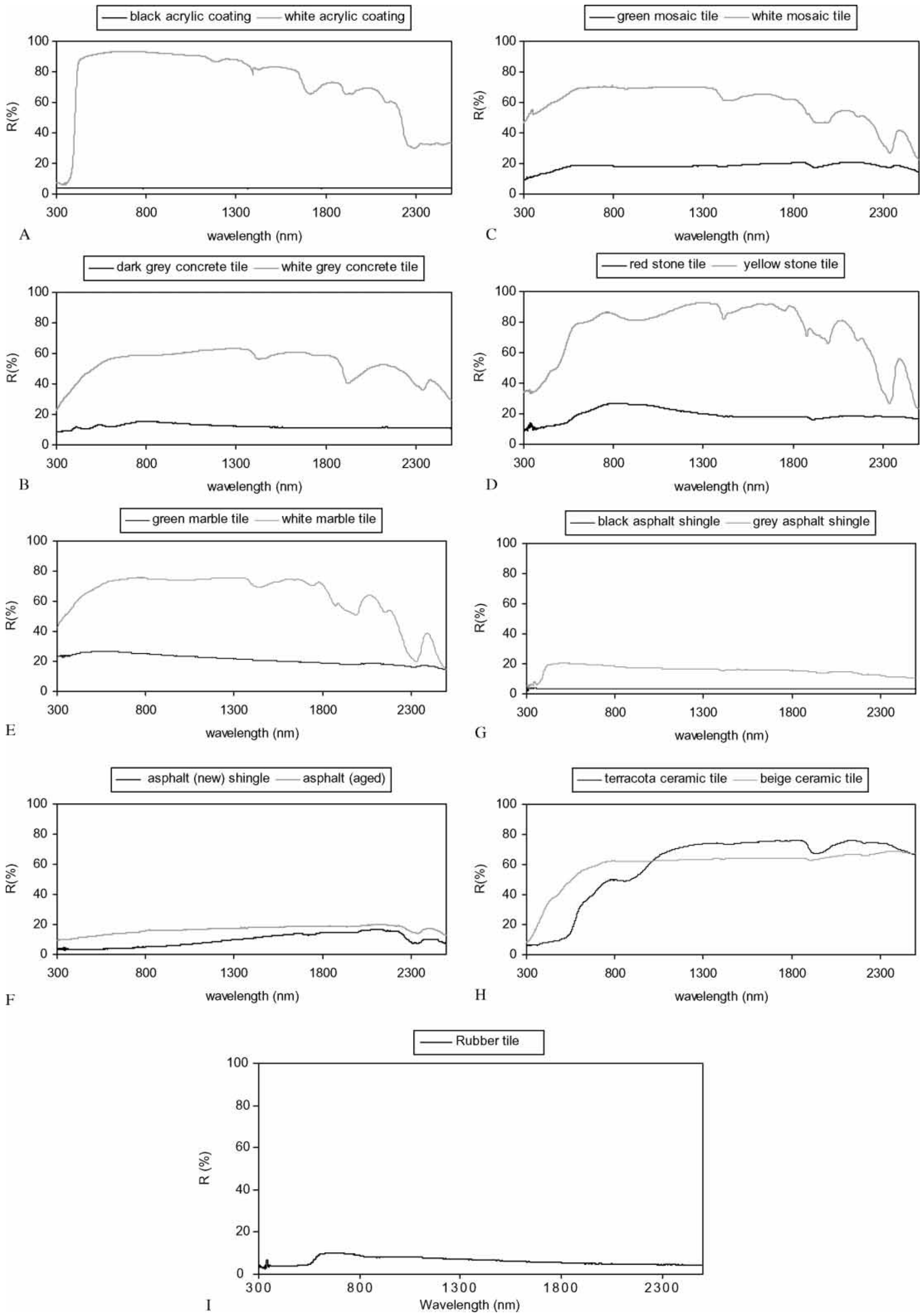

Figure 8. The measured spectral reflectance of the material with the highest and lowest reflectance for each material category (A-I) for all the tested materials.

$5.6685 \times 10^{-8}\,\mathrm{W/m^2\,K^4}$, T_s the equilibrium surface temperature (K), T_{sky} the effective radiant sky temperature ($T_{sky} = 300\,\mathrm{K}$), h_c the convection coefficient ($h_c = 12\,\mathrm{W/m^2\,K}$) and T_a the air temperature ($T_a = 310\,\mathrm{K}$).

Finally, in order to evaluate the thermal performance of the materials, the solar reflectance index (SRI) was calculated based on the previous measurements. It is a measure of the surface's ability to reject solar heat, as shown by a small temperature rise. It is defined so that a standard black (reflectance 0.05, emittance 0.90) is 0 and a standard white (reflectance 0.80, emittance 0.90) is 100. Materials with the highest SRI values are the coolest choices. Due to the way SRI is defined, particularly hot materials can even take slightly negative values, and particularly cool materials can even exceed 100. The calculations were performed according to the ASTM E1980-01 and Equation (19):

$$\mathrm{SRI} = 100\frac{T_b - T_s}{T_b - T_w}, \tag{19}$$

where T_b, T_w and T_s are the calculated equilibrium temperatures of a black surface, a white surface and the surface under consideration. Figure 7 describes the minimum and maximum values of the calculated SRI for each material category.

As expected for all material categories, white and light-coloured materials have higher values of SR and lower surface temperatures. For example, a white coating that is characterised by an SR of 0.83 reaches a maximum surface temperature under peak solar conditions that is by 40°C lower than the corresponding maximum temperature of a black coating with an SR of 0.04. For different materials of the same colour, for example, a white marble tile has a higher SR (0.73) than a white concrete tile (SR = 0.55). In general, the best performing materials according to Table 6 and Figure 7 are the light-coloured coatings, stone, marble, membranes and mosaic. The worst performing materials are asphalt and asphalt shingles. Even a light-coloured asphalt shingle has a very low SR (0.18) and therefore reaches a high surface temperature.

The results of the spectrophotometric measurements are shown in Figure 8 (A-I). Each chart contains the measured spectral reflectance for the material with the higher and lower value of SR for a particular material category. Most of the materials, mainly the dark-coloured ones, are characterised by low near-infrared reflectance. Taking into account that about half of the solar power arrives as near-infrared radiation (ASTM Standard G159-91) and that pigments are the primary factor affecting the reflectance of a coating (Wake and Brady 1992), using near-infrared reflective pigments would result in increasing the SR of the materials without changing their colour. For example, using a near-infrared reflective black pigment (Levinson *et al.* 2005a, 2005b) to manufacture a coating could result in an SR increase by 0.22 (Synnefa *et al.* 2007).

All the measured and calculated information about the 87 tested building and paving materials have been used to create a database of optical and thermal data in order to characterise the materials as cool, i.e. having a high SR and infrared emittance, or warm. Choosing cool materials for the urban environment instead of warm could improve building comfort and reduce cooling energy use, and at city scale, it could contribute to the reduction of the air temperature due to heat transfer phenomena and therefore improve outdoor thermal comfort and reduce the heat island effect.

6. Conclusions

The SUHI effect is clearly observed on satellite images of both day and night. Specifically, during daytime in metropolitan Athens, a negative SUHI is developed where open, non-urban surfaces in the city surroundings are warmer than urban surfaces. As urban areas are characterised by compact and high buildings, they have a high thermal mass (building mass per unit area) in contrast to non-urban areas that are characterised by a small thermal mass. Thus, during daytime, there is a lag in solar heating of urban areas due to the thermal properties of the building materials. On the other hand, at night, the thermal pattern is inversed and an intense surface UHI is developed. Non-urban surfaces cool more rapidly than urban surfaces as building materials are stores of heat. Vegetation and surface emissivity appears to have a cooling effect on urban surface temperatures. Thus, during night-time, the more vegetated and of higher surface emissivity urban suburbs in the NE of Athens are cooler than the SW suburbs.

In order to characterise commonly used materials as cool or warm a database of optical and thermal properties of 87 paving and building materials used in the urban fabric of Athens has been created. The spectral reflectance and the infrared emittance of the samples were measured and their SR and SRI were calculated. It was found that the coolest options are light-coloured coatings, marble, stone and membranes. Additionally, it was demonstrated that many dark-coloured materials are characterised by low near-infrared reflectance. This indicates that the use of near-infrared reflective pigments for their construction could increase significantly their SR without compromising their colour.

This study can assist architects, building physicists, engineers, etc., in the selection of more appropriate materials for outdoor urban applications contributing to the mitigation of the heat island effect.

Acknowledgements

This study was performed with funding provided by the General Secretariat for Research and Technology of the Hellenic Republic Ministry of Development in Greece. Knowledge transfer and guidance from the Lawrence Berkeley National Laboratory is gratefully acknowledged.

References

Akbari, H., *et al.*, 2004. Cool colored materials for roofs. *ACEEE summer study on energy efficiency in buildings*, Asilomar Conference Center in Pacific Grove, CA. American Council for an Energy Efficient Economy.

Akbari, H., *et al.*, 1997. Peak power and cooling energy savings of high albedo roofs. *Energy and Buildings – Special Issue on Urban Heat Islands and Cool Communities*, 25 (2), 117–126.

Asaeda, T., Ca, V.T., and Wake, A., 1996. Heat storage of pavement and its effect on the lower atmosphere. *Atmospheric Environment*, 30 (3), 413–427.

ASTM E1980-01. Standard practice for calculating solar reflectance index of horizontal and low-sloped opaque surfaces.

ASTM Standard E903-96. Standard test method for solar absorptance, reflectance and transmittance of materials using integrating spheres.

ASTM Standard G159-91. Standard tables for references solar spectral irradiance at air mass 1.5: direct normal and hemispherical for a 37° tilted surface.

Bretz, S. and Akbari, H., 1997. Long-term performance of high albedo roof coatings. *Energy and Buildings*, 25, 159–167.

Cartalis, C., *et al.*, 2001. Modifications in energy demand in urban areas as a result of climate changes: an assessment for the southeast Mediterranean region. *Energy Conservation and Management*, 42, 1647–1656.

Caselles, V., *et al.*, 1991. Analysis of the heat island effect of the city of Valencia, Spain, through air-temperature transects and NOAA satellite data. *Theoretical and Applied Climatology*, 43, 195–203.

Chander, G. and Markham, B., 2003. Revised Landsat-5 TM radiometric calibration procedure and post-calibration dynamic ranges. *IEEE Transactions on Geoscience and Remote Sensing*, 41, 2674–2677.

Chavez, P.S., 1988. An improved dark-object subtraction technique for atmospheric scattering correction of multispectral data. *Remote Sensing of the Environment*, 24, 459–447.

Chavez, P.S., 1996. Image-based atmospheric corrections revisited and improved. *Photogrammetric Engineering and Remote Sensing*, 62, 1025–1036.

Chrysoulakis, N. and Cartalis, C., 2002. Improving the estimation of land surface temperature for the region of Greece: adjustment of a split window algorithm to account for the distribution of precipitable water. *International Journal of Remote Sensing*, 23, 871–880.

Doulos, L., Santamouris, M., and Livada, I., 2004. Passive cooling of outdoor urban spaces. The role of materials. *Solar Energy*, 77, 231–249.

Dousset, B. and Gourmelon, F., 2003. Satellite multi-sensor data analysis of urban surface temperatures and landcover. *Journal of Photogrammetry and Remote Sensing*, 58, 43–54.

Earth Remote Sensing Data Center (ERSDAC), 2001. ASTER user's guide.

European Commission, 1994. CORINE land cover. Technical guide, EUR 12585 EN, OPOCE, Luxembourg.

Gallo K.P., *et al.*, 1995. Assessment of urban heat islands: a satellite perspective. *Atmospheric Research*, 37, 37–43.

Hung, T., *et al.*, 2006. Assessment with satellite data of the urban heat island effects in Asian mega cities. *International Journal of Applied Earth Observation and Geoinformation*, 8, 34–48.

Jiménez-Munõz, J.C. and Sobrino, J.A., 2003. A generalized single-channel method for retrieving land surface temperature from remote sensing data. *Journal of Geophysical Research*, 108 (D22), 4688, doi:10.1029/2003JD003480.

LBNL. http://eetd.lbl.gov/coolroof/.

Levinson, R., Berdahl, P., and Akbari, H., 2005a. Spectral solar optical properties of pigments. Part I: model for deriving scattering and absorption coefficients from transmittance and reflectance measurements. *Solar Energy Materials and Solar Cells*, 89, 319–349.

Levinson, R., Berdahl, P., and Akbari, H., 2005b. Spectral solar optical properties of pigments. Part II: survey of common colorants. *Solar Energy Materials and Solar Cells*, 89, 351–389.

Liang, S., 2006. Narrowband to broadband conversions of land surface albedo: I. Algorithms, *Remote Sensing of Environment*, 76, 213–238.

Livada, *et al.*, 2002. Determination of places in the great Athens area where the heat island is observed. *Theoretical and Applied Climatology*, 71, 219–230.

Mihalakakou, G., *et al.*, 2004. Simulation of the urban heat island phenomenon in Mediterranean climates. *Pure and Applied Geophysics*, 161, 429–451.

Nichol, J.E., 2005. Remote sensing of urban heat islands by day and night. *Photogrammetric Engineering and Remote Sensing*, l71, 613–621.

Parker, D.S., *et al.*, 2000. Laboratory Testing of the Reflectance Properties of Roofing Material. *FSEC-CR-670-00*, Florida Solar Energy Centre, Cocoa, FL.

Prado, R.T.A. and Ferreira, F.L., 2005. Measurement of albedo and analysis of its influence the surface temperature of building roof materials. *Energy and Buildings*, 37, 295–300.

Rosenfeld, A.H., *et al.*, 1996. Policies to reduce heat islands: magnitudes of benefits and incentives to achieve them. *Proceedings of the 1996 ACEEE summer study on energy efficiency in buildings*, Vol. 9.

Roth, M., Oke, T.R., and Emery, W.J., 1989. Satellite-derived urban heat islands from 3 coastal cities and the utilization of such data in urban climatology. *International Journal of Remote Sensing*, 10, 1699–1720.

Sailor, D.J., 1995. Simulated urban climate response to modifications in surface albedo and vegetative cover. *Journal of Applied Meteorology*, 34 (7), 1694–1704.

Santamouris, M., *et al.*, 2001. On the impact of urban climate on the energy consumption of buildings. *Solar Energy*, 70, 201–216.

Simpson, J.R. and McPherson, E.G., 1997. The effect of roof albedo modification on cooling loads of scale residences in Tucson, Arizona. *Energy and Buildings*, 25, 127–137.

Stathopoulou, M. and Cartalis, C., 2001. Use of satellite remote sensing in support of urban heat island studies. *Advances in Building Energy Research*, 1, 203–212.

Stathopoulou, M., Cartalis, C., and Petrakis, M., 2007. Integrating Corine land cover data and Landsat TM for surface emissivity definition: application to the urban area of Athens, Greece. *International Journal of Remote Sensing*, 28, 3291–3304.

Synnefa, A., Santamouris, M., and Apostolakis, K., 2007. On the development, optical properties and thermal performance of cool colored coatings for the urban environment. *Solar Energy*, 81, 488–497.

Taha, H., Chang, S., and Akbari, H., 2000. Meteorological and air impacts of heat island mitigations measures in three U.S. cities. LBNL report 44222.

Taha, H., Hammer, H., and Akbari, H., 2002. Meteorological and air impacts of increased urban surface albedo and vegetative cover in the Greater Toronto Area, Canada. LBNL report 4921.

Voogt, J.A. and Oke, T.R., 2003. Thermal remote sensing of urban climates. *Remote Sensing of Environment*, 86, 370–384.

Wake, L.V. and Brady, R.F., 1992. Principles and formulations for organic coatings with tailored infrared properties. *Progress in Organic Coatings*, 20, 1–25.